A Dual-Frequency Modular Wireless Power Transfer System for Auxiliary Power Supply of Power Electronics Converters

Wenxuan Pan, Zhongjin Huang, Rongbin Liu, Hongmin Tang, Ronghuan Xie, *Graduate Student Member, IEEE*, Yizhan Zhuang, *Member, IEEE*, and Yiming Zhang, *Senior Member, IEEE*

***Abstract*—In some industrial application scenarios, multiple constant-voltage (CV) outputs with galvanic isolation are required. Selective power transfer among the CV outputs can enable its flexibility. This article proposes a modular single-channel wireless power transfer system for industrial power supply with a dual-frequency hybrid compensation topology. The series–series topology is adopted for CV outputs at the two CV output frequency points. The bandstop filter with a parallel resonant network is designed to filter the undesired frequency component, and the series–series–parallel resonant network is formed to avoid the impact of the bandstop filter on the desired frequency component. In this way, selective power transfer with CV outputs can be achieved by changing the working frequency. The mathematical model of the proposed compensation topology is established and analyzed. The transmission coils and the compensating inductors are integrated to achieve a compact structure. The design principles of the coupler parameters are proposed, and a design example is given. An experimental prototype is built to verify the theoretical analysis. The system realizes CV outputs and supplies power to different loads at different working frequencies, with an average transfer efficiency of 85.23% and a maximum output power of 85.95 W.**

***Index Terms*—Auxiliary power supply (APS), constant voltage (CV), dual frequency, modularity, wireless power transfer (WPT).**

I. Introduction

WIRELESS power transfer (WPT) can realize the energy transfer from the power source to the load without direct electrical contact. Compared with the traditional wired energy transfer, it can effectively avoid the problems of spark and electric shock and has advantages in improving the reliability, safety, convenience, and extending the service life of the equipment [1], [2], [3]. Depending on the different transfer mechanisms, WPT can be divided into the electric-field-coupled WPT and the magnetically coupled resonant WPT [4], [5], [6]. Today, WPT has been widely used in the applications of implantable medical devices, consumer electronics, underwater applications, electric vehicles, rail transit, etc. [7], [8], [9], [10].

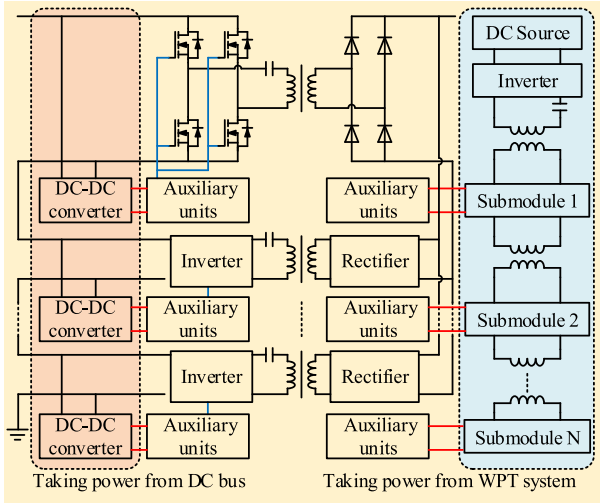

Fig. 1. SSTs with APSs.

In medium- and high-capacity power applications, such as modular multilevel converters, high-voltage dc circuit breakers, solid-state transformers (SSTs), and so on, multiple power electronic switches or converters are connected in parallel or series to handle voltage or high current stresses. Accordingly, multiple constant-voltage (CV) outputs for low-voltage auxiliary power supplies (APSs) of the drive circuits, controllers, and sensors are required [11]. Take the SST as an example. The SST is widely used in medium- and high-voltage applications due to the benefits of high working frequency and power density. The SST topologies typically adopt an input-series output-parallel arrangement, which can transform high-voltage low-current input to high-current low-voltage output. Multiple APSs with galvanic isolation are needed to supply power for the driving circuits of each inverter, as shown in Fig. 1. The traditional power supply solution is to use an isolated dc–dc converter, but it

Manuscript received 5 March 2024; revised 25 April 2024; accepted 26 May 2024. Date of publication 31 May 2024; date of current version 16 July 2024. This work was supported in part by the National Natural Science Foundation of China under Grant 52107183 and in part by the Natural Science Foundation of Fujian Province under Grant 2022J06011. Recommended for publication by Associate Editor D. Dujic. *(Corresponding authors: Yizhan Zhuang; Yiming Zhang.)*

The authors are with the School of Electrical Engineering and Automation, Fuzhou University, Fuzhou 350108, China (e-mail: 220120033@fzu.edu.cn; 220120026@fzu.edu.cn; 220127070@fzu.edu.cn; 220127089@fzu.edu.cn; 230127018@fzu.edu.cn; zyz_joe@fzu.edu.cn; zym@fzu.edu.cn).

Color versions of one or more figures in this article are available at https://doi.org/10.1109/TPEL.2024.3407880.

Digital Object Identifier 10.1109/TPEL.2024.3407880

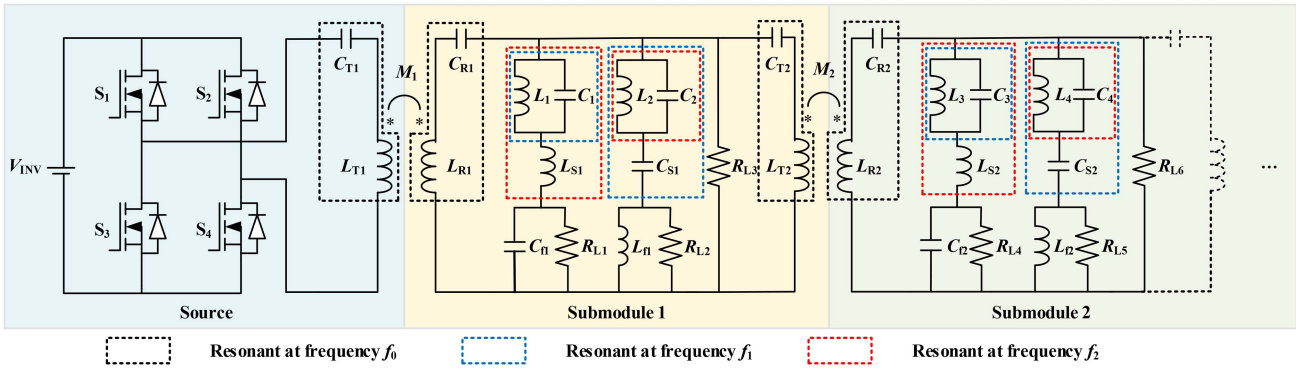

Fig. 2. Modular single-channel dual-frequency WPT system with multiple selective CV outputs.

requires additional control circuits and input voltage unbalance protection circuits. Meanwhile, the use of magnetic cores leads to the problem of high cost and large size.

The WPT technology can provide a flexible, reliable, and effective solution for power supply. Some WPT topologies have CV output characteristics, eliminating the need for control and protection circuits, and the air gap guarantees the realization of electrical isolation without magnetic cores. Therefore, the WPT system with multiple outputs is a desirable alternative. Using one transmitting coil to supply power for multiple receiving coils can be one solution, but it requires the decoupling of multiple receiving coils to achieve independent control [12]. A domino WPT system with power relay coils is another solution with each relay coil connected to a load. Each relay coil not only receives power to the load but also transmits power to the next relay coil. Thus, multiple-load transfer can be realized over different charging distances. Cho et al. [13] proposed a capacitively tuned relay structure. The system adds an extra shunt capacitance. By changing the capacitance, different power distributions at variable loads and distances can be satisfied. Two coils can be combined as a relay unit, decoupled by ferrite inserted between the coils, or using decoupled coils, to serve as the receiver and the transmitter, respectively. The *LCC*-S compensation can be utilized to realize CV output [14]. Cheng et al. [15] proposed an asymmetrical coil design, which reduced the number of compensating elements.

To flexibly use these multiple CV outputs, selective power transfer or controlled power distribution is preferred [16]. Tian et al. [17] controlled and regulated the magnetic field in the powering area to meet different output power requirements. A dual-working-frequency circuit is used to achieve an independent adjustment for output powers and prevent interference among outputs [18]. Cai et al. [19] employed capacitance tuning to provide sufficient freedom in gain regulation. Without complex control mechanisms, variable compensations, and extra switches, the multifrequency WPT system is promising research [20].

This article proposes a modular dual-frequency WPT system with multiple selective CV outputs. Section II presents the mathematical model of the compensation topology. In Section III, the magnetic couplers are simulated and designed. The effectiveness of the proposed system is experimentally verified in Section IV. Finally, Section V concludes this article.

II. Proposed Multi-CV-Output System

The proposed modular dual-frequency topology with multiple selective CV outputs is shown in Fig. 2. S_1–S_4 are the power metal–oxide–semiconductor field-effect transistors (MOSFETs) of the inverter. V_{INV} represents the dc voltage of the inverter. L_{T1}, L_{T2}, L_{R1}, and L_{R2} are the self-inductances of the transmission coils. M_1 and M_2 are the mutual inductances among the coils. C_{T1}, C_{T2}, C_{R1}, and C_{R2} are the compensation capacitances of the transmission coils. L_1–L_4, C_1–C_4, L_{S1}, L_{S2}, C_{S1}, and C_{S2} constitute the bandstop filters. L_{f1}, L_{f2}, C_{f1}, and C_{f2} are the compensation inductances and capacitances to achieve zero phase angle (ZPA). R_{L1}–R_{L6} are the load resistances. f_1 and f_2 are the two working frequencies of the system.

The components from the receiving coil L_{R1} to the next transmitting coil L_{T2} constitute a submodule, with three loads connecting to three branches. The proposed system can be flexibly extended by adding more submodules.

A. Realization of CV Outputs at f_1 and f_2

For the series–series (S–S) topology, assume that the parameters of the transmitting and receiving coils are identical, namely

$$\begin{cases} L = L_{T1} = L_{R1} = L_{T2} = L_{R2} \\ C = C_{T1} = C_{R1} = C_{T2} = C_{R2} \\ M = M_1 = M_2 = kL \end{cases} \tag{1}$$

where k is the coupling coefficient of the coils.

The decoupling equivalent circuit and the fundamental harmonics approximation (FHA) method are used to obtain the two CV output points for the S–S topology. Its topology and T-type equivalent circuits are depicted in Fig. 3. Without changing the connection, coupling coils can be decoupled using T-type equivalent circuits. The original resonant frequency can be expressed as

$$f_0 = \frac{1}{2\pi\sqrt{LC}}. \tag{2}$$

In Fig. 3(b), when (L+M) resonates with C, the output voltage is equal to the input voltage, regardless of the load resistance,

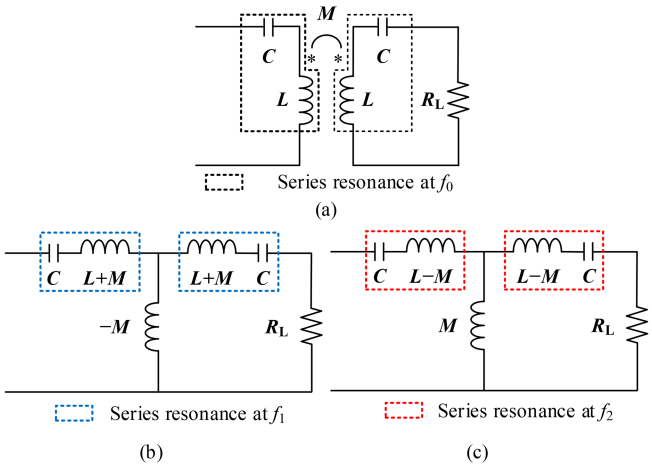

Fig. 3. S–S topology and its T-type equivalent circuits. (a) S–S topology. (b) T-type equivalent circuits at f_1. (c) T-type equivalent circuits at f_2.

achieving a load-independent CV output. The resonant frequency can be expressed as

$$f_1 = \frac{1}{2\pi\sqrt{(L+M)C}} = \frac{f_0}{\sqrt{1+k}}. \tag{3}$$

Similarly, in Fig. 3(c), when (L−M) resonates with C, the output voltage is equal to the input voltage, regardless of the load resistance, achieving a load-independent CV output. The resonant frequency can be expressed as

$$f_2 = \frac{1}{2\pi\sqrt{(L-M)C}} = \frac{f_0}{\sqrt{1-k}}. \tag{4}$$

According to (3) and (4), the relationship between the two CV output frequency points can be obtained as

$$f_2 = \sqrt{\frac{1+k}{1-k}} f_1. \tag{5}$$

For coupled coils with fixed positions, these two frequency points are constant. Thus, these two frequency points can be utilized to generate CV outputs.

B. Realization of ZPA

The two CV points of the S–S topology are employed to realize CV outputs as mentioned previously. However, there are two disadvantages: 1) there is large reactive power due to the existence of the parallel branches of either $-M$ in Fig. 3(b) or M in Fig. 3(c), which indicates that ZPA is not achieved, and the transfer efficiency and power transfer capability will be affected; and 2) in Fig. 3(b), the input impedance of the WPT system is capacitive, which means that zero-voltage switching would not be achieved, affecting the transfer efficiency and the safety operation of the inverter.

Therefore, an improvement is made by connecting the extra compensating inductances or capacitances in parallel at the CV output ports of the load to form a series–series–parallel (S-SP) compensation topology, as given in Fig. 4.

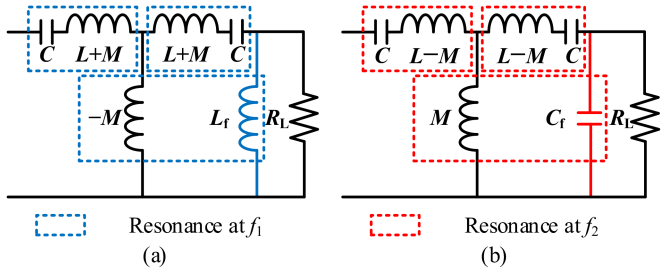

Fig. 4. Realization of ZPA by adding compensating inductance or capacitance. (a) Adding an inductor for $-M$. (b) Adding a capacitor for M.

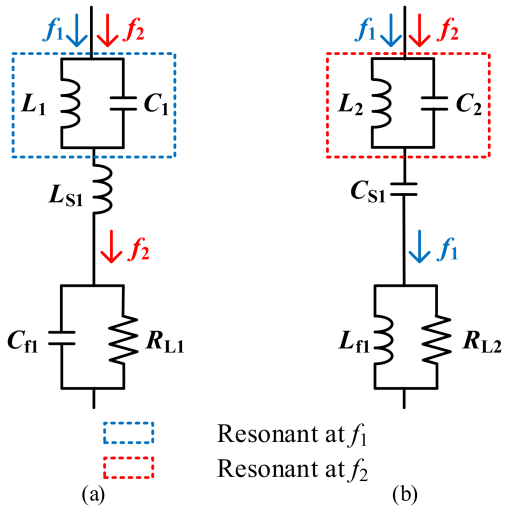

Fig. 5. Bandstop filters. (a) Frequency f_2-pass filter. (b) Frequency f_1-pass filter.

The relationships of the compensation networks can be expressed as

$$\begin{cases} -j2\pi f_1 M + j2\pi f_1 L_f = 0 \\ j2\pi f_2 M + \frac{1}{j2\pi f_2 C_f} = 0 \end{cases}. \tag{6}$$

C. Realization of Selective Power Transfer

As mentioned previously, CV outputs with ZPA can be achieved at f_1 and f_2. To achieve selective power transfer, the load branches of the two frequency points should be independent from each other. To achieve this target, bandstop filters are employed to stop the undesired frequency component on the load branch, as shown in Fig. 5. To eliminate the impact of the bandstop filter on the desired CV output, the series resonance can be formed with the bandstop filter. Therefore, the compensation network needs to meet the following conditions.

1) L_1 (L_2) and C_1 (C_2) are in parallel resonance (equivalent to open circuit) at frequency f_1 (f_2) to stop the f_1 (f_2) component flowing through this branch.
2) L_1 (L_2), C_1 (C_2), and L_{S1} (C_{S1}) are in series resonance (equivalent to short circuit) at frequency f_2 (f_1) to allow the f_2 (f_1) component flowing through this branch.

In this way, the component of frequency f_1 will only flow through the branch of C_{S1}, supplying power to R_{L2}; the component of frequency f_2 will only flow through the branch of

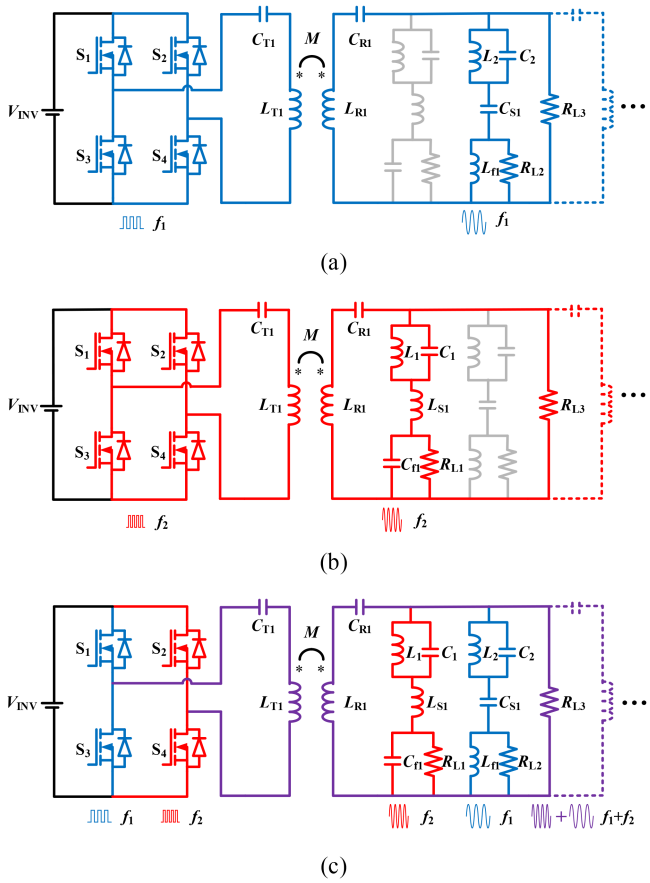

Fig. 6. (a)–(c) Equivalent circuit of three different operating modes.

L_{S1}, supplying power to R_{L1}. Thus, selective power transfer is realized by changing the working frequency to f_1 or f_2. The resonant relationships can be expressed as

$$\begin{cases} j2\pi f_1 L_1 + \frac{1}{j2\pi f_1 C_1} = 0 \\ j2\pi f_2 L_2 + \frac{1}{j2\pi f_2 C_2} = 0 \\ j2\pi f_1 L_2 \parallel \frac{1}{j2\pi f_1 C_2} + \frac{1}{j2\pi f_1 C_S} = 0 \\ j2\pi f_2 L_1 \parallel \frac{1}{j2\pi f_2 C_1} + j2\pi f_2 L_S = 0. \end{cases} \tag{7}$$

Using (5) and (7) yields

$$L_S = \frac{L-M}{2M} L_1 = \frac{1-k}{2k} L_1 \tag{8}$$

$$C_S = \frac{2M}{L-M} C_2 = \frac{2k}{1-k} C_2. \tag{9}$$

D. Operating Modes

Correspondingly, the system has three operating modes.

1) *Mode 1:* The inverter operates at the switching frequency f_1, supplying power to the loads R_{L2}, R_{L5}, R_{L3}, and R_{L6}.
2) *Mode 2:* The inverter operates at the switching frequency f_2, supplying power to the loads R_{L1}, R_{L4}, R_{L3}, and R_{L6}.
3) *Mode 3:* One arm of the inverter operates at the switching frequency f_1 and the other at f_2.

The equivalent circuits of the three operating modes are shown in Fig. 6. Note that in Mode 3, the voltage and current in the system are superimposed on both the frequencies, supplying power to all the loads.

The FHA method is utilized. V_S is the RMS value of the inverter output voltage. When the inverter is operated as a full bridge at only one frequency, V_S can be calculated as

$$V_S = \frac{2\sqrt{2}}{\pi} V_{\text{INV}}. \tag{10}$$

The output voltages in Mode 1 can be expressed as

$$\begin{aligned} V_{RL(3n+1)} &= 0, V_{RL(3n+2)} \\ &= V_{RL(3n+3)} = V_S^{(1)}, \quad n = 0, 1, 2 \ldots. \end{aligned} \tag{11}$$

The output voltages in Mode 2 can be expressed as

$$\begin{aligned} V_{RL(3n+2)} &= 0, V_{RL(3n+1)} \\ &= V_{RL(3n+3)} = V_S^{(2)}, \quad n = 0, 1, 2 \ldots. \end{aligned} \tag{12}$$

The output voltages in Mode 3 can be expressed as

$$\begin{cases} V_{RL(3n+1)} = V_S^{(2)}/2 \\ V_{RL(3n+2)} = V_S^{(1)}/2 \\ V_{RL(3n+3)} = \sqrt{\left(V_S^{(1)}/2\right)^2 + \left(V_S^{(2)}/2\right)^2}, \end{cases} n = 0, 1, 2 \ldots \tag{13}$$

where the superscript (x) $(x = 1, 2)$ represents the dual working frequencies.

The system efficiency η can be defined as

$$\eta = \frac{P_{\text{out}}}{P_{\text{in}}} = \frac{\sum \left(V_{RLn}^2 / R_{Ln}\right)}{V_{\text{INV}} I_{\text{dc}}}. \tag{14}$$

E. Impact of Parasitic Resistances

In practical systems, the parasitic resistance cannot be ignored. The quality factors of L_{Tn}, L_{Rn}, L_n, L_{Sn}, and L_{fn} at f_1 frequency are defined as Q_{Tn}, Q_{Rn}, Q_n, Q_{Sn}, and Q_{fn}, respectively. The parasitic resistance can be expressed as

$$r_i = 2\pi f_1 L_i / Q_i. \tag{15}$$

Due to the modular design, these parameters are identical, and therefore, they have the same quality factor. However, considering that the inductors have different roles in the system: transmission coils and compensation inductors, Q is divided into Q_a and Q_b correspondingly. $Q_{Tn} = Q_{Rn} = Q_a$; $Q_n = Q_{Sn} = Q_{fn} = Q_b$. The parasitic resistance influences the CV outputs. Given the parasitic resistance, the analytical expressions of the outputs are complicated. Thus, the output voltage variations against the quality factors can be simulated by bringing the design parameters into the model. The trend of output voltage for different quality factors is shown in Fig. 7. Setting $f_1 = 200$ kHz, $n = 3$, the loads are the same and varied from 50 to 150 Ω. For comparison purposes, normalized load resistances and voltages are used with basic values defined as

$$V_b = V_S, R_b = R_{L\text{MAX}}. \tag{16}$$

Due to the presence of parasitic parameters, the output voltage is not a constant value but increases with the load resistance.

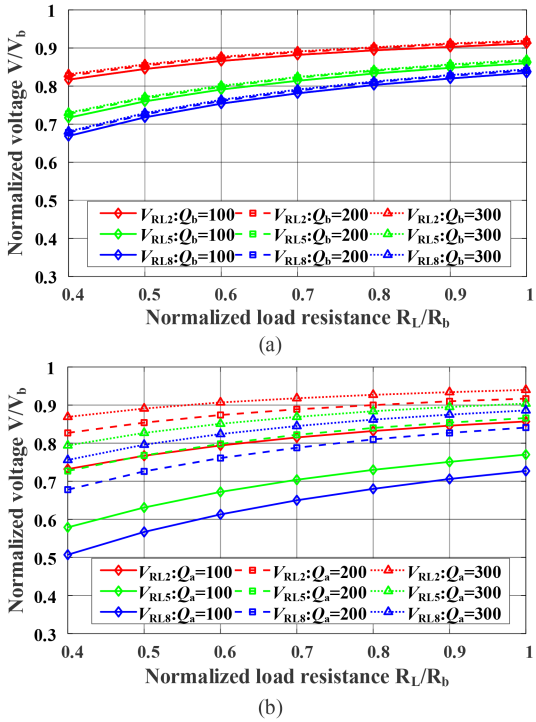

Fig. 7. Output voltage variations against the quality factors at (a) $Q_a = 200$ and (b) $Q_b = 200$.

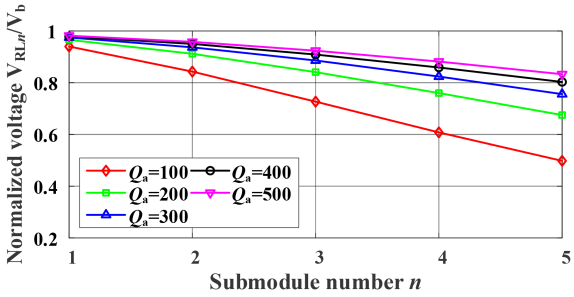

Fig. 8. Output voltage variations of the last submodule against submodule number.

With an identical quality factor, the output voltage of the backward stage is smaller than that of the preceding stage; on the other hand, the amplitude of the output voltage increases with the increasing quality factors. The parasitic resistance in the filter network (related to the quality factor Q_b) has a limited effect on the output voltage, while the parasitic resistance on the transmission coil (related to the quality factor Q_a) has a larger effect on the output voltage at low load resistances. High quality factor contributes to reducing the impact of parasitic resistance on CV output. Parasitic resistance led to a voltage drop between the source and the loads, preventing the system from endlessly increasing the submodule number to guarantee adequate voltage for all the loads. Otherwise, a significant increase in the output voltage of the inverter is required, potentially causing the loads near the inverter to overvoltage. Fig. 8 shows the last output voltage in relation to the submodule number. The output voltage of the last submodule is decreasing as the number increases.

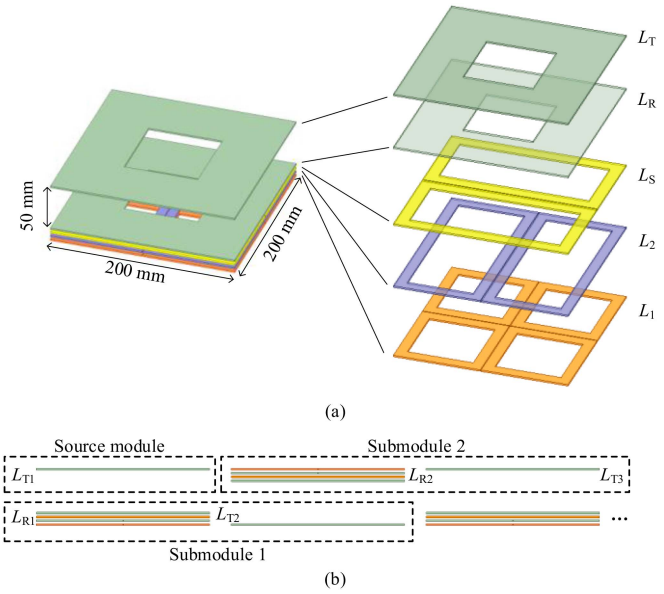

Fig. 9. Proposed magnetic couplers. (a) Structure. (b) Placement.

However, the trend of voltage drop becomes slow with a high coil quality factor. With smaller n, voltage drop does not need to be dealt with. When n is large, the voltage drop can be effectively mitigated by increasing the coil quality factor. To determine the load module number n, a threshold value is set such that when the normalized output falls below this value, the load module cannot be increased. In summary, a high quality factor is essential.

III. Magnetic Couplers

As can be seen from Fig. 2, there are multiple coils in the proposed system. Apart from the power transmission coils L_{T1}, L_{R1}, L_{T2}, and L_{R2}, there are also compensating inductances L_1, L_2, L_{S1}, L_{f1}, L_3, L_4, L_{S2}, and L_{f2}. To achieve a compact structure, these coils can be integrated when they are decoupled from each other.

A. Magnetic Integration Design

The proposed magnetic couplers are shown in Fig. 9(a). The coils are with a size of 200 × 200 mm. The transfer distance is 50 mm. Integrate the compensating inductors in the coupling mechanism to achieve a compact structure. To realize the decoupling between the transmission coils and the compensating inductors, the four mutually decoupled coils, namely, the unipolar coil, the bipolar coils along two perpendicular directions, and the quadrupole coil, are utilized. To achieve decoupling among adjacent magnetic couplers, the coils within a submodule are placed side by side, and the adjacent submodules are overlapped with each other, as shown in Fig. 9(b). The transmission coils are designed as the unipolar coils. L_2 and L_{S1} are designed as the bipolar coils along two perpendicular directions. L_1 is designed as the quadrupole coil. These coils are decoupled from each other. L_{f1} is designed as a lumped inductor.

TABLE I
SELF-INDUCTANCE OF L_1 AND L_S FOR DIFFERENT TURNS

Turns	L_1 (μH)	1.081*L_1 (μH)	L_S (μH)
5	24.269	26.240	20.301
6	31.634	34.203	26.825
7	39.215	42.400	33.800
8	46.381	50.147	41.065
9	53.876	58.250	48.348
10	60.858	65.799	55.796

TABLE II
SELF-INDUCTION VARIATION WHEN L_2 CHANGES

Turns of L_2	L_1 (μH)	1.081*L_1 (μH)	L_S (μH)	Difference (nH)
5	32.463	35.099	35.216	116.90
6	32.064	34.668	34.644	23.31
7	31.686	34.259	34.176	85.558
8	32.107	34.714	34.640	73.99
9	32.265	34.884	34.651	233.29
10	31.742	34.319	34.250	69.27

B. Design Example

The difficulty in the design of the coupling mechanism parameters is to make the relationship among the self-inductances of the compensation coil satisfy (8). To illustrate the design principle of the coupler parameters, a design example is given.

The parameters of L_T and L_R must first be determined. The mutual inductance of the S-SP topology determines the reactive current flowing through the coils. As the mutual inductance increases, the reactive current decreases. With a fixed coil size and type as well as the transfer distance, the mutual inductance is only related to the number of turns. The turns of L_1, L_2, L_S, and L_T (L_R) are assigned as 5, 5, 5, and 30, respectively. Running the electromagnetic simulation model, the parameters can be obtained that $L_T = 162.50$ μH, $L_R = 162.039$ μH, and $M = 51.31$ μH. Substituting the data into (5) and (8), one can get $f_2 \approx 1.387 f_1$, and $L_S \approx 1.081 L_1$. L_1 is assigned as a quadrupole coil, and L_S is assigned as a bipolar coil. The change in the number of turns has a slight effect on the self-inductance of other coils, which can be disregarded. Table I shows the self-inductance of L_1 and L_S for different turns.

When L_1 has six turns and L_S has seven turns, (8) is satisfied. Therefore, the turn numbers of L_1 and L_S can be determined. When L_2 changes, the situation of self-inductance is shown in Table II. The best performance is achieved when L_2 is assigned as six turns.

At this point, all the parameters of the couplers are determined, and the relationships satisfy the requirements. The flowchart of the magnetic coupler design is shown in Fig. 10.

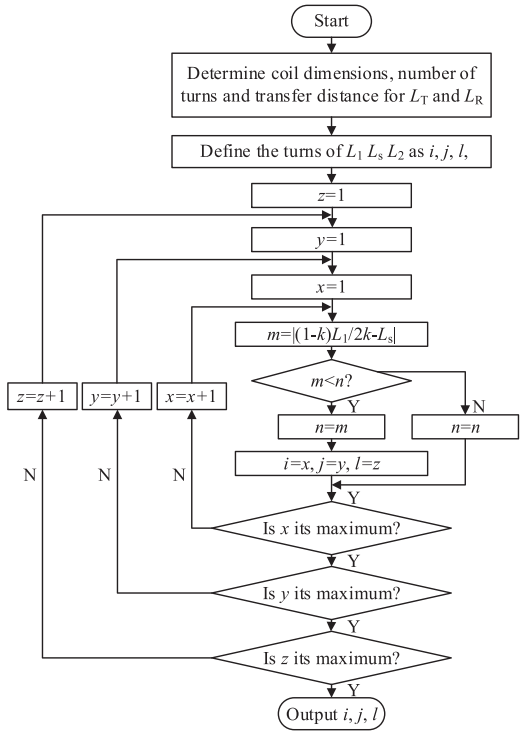

Fig. 10. Flowchart of magnetic coupler design.

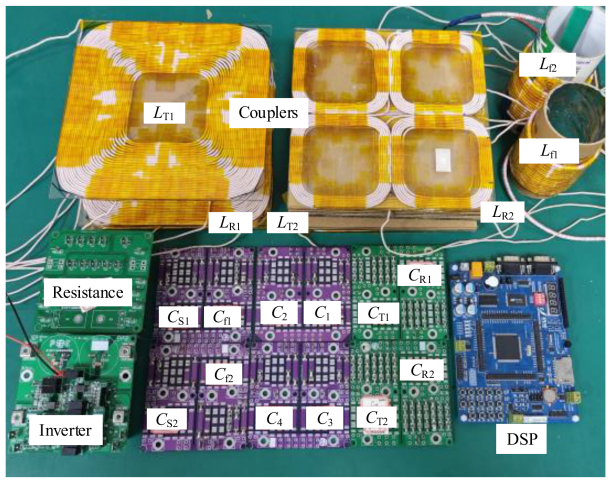

Fig. 11. Photograph of the experimental setup.

IV. EXPERIMENTAL VERIFICATION

According to the relationships of the compensation networks in Section II and the design results in Section III, a power relay system containing two subunits is built, as shown in Fig. 11. All coils and lumped inductors were wound from 0.1 mm × 220 strands of Litz wires. The H-bridge inverter consists of four silicon carbide MOSFETs. Thick-film noninductive resistors are selected as the load. Because of the characteristics of the S–S topology, high working frequencies facilitate reduced current stress as well as access to more subunits. If the working frequency is too high, the parameter accuracy of the compensation elements may not meet the requirement, resulting in system detuning. Therefore, the working frequency of f_1 is set to 200 kHz. Considering the tiny inductance present in the connected wires, the capacitance is adjusted to achieve better experimental results,

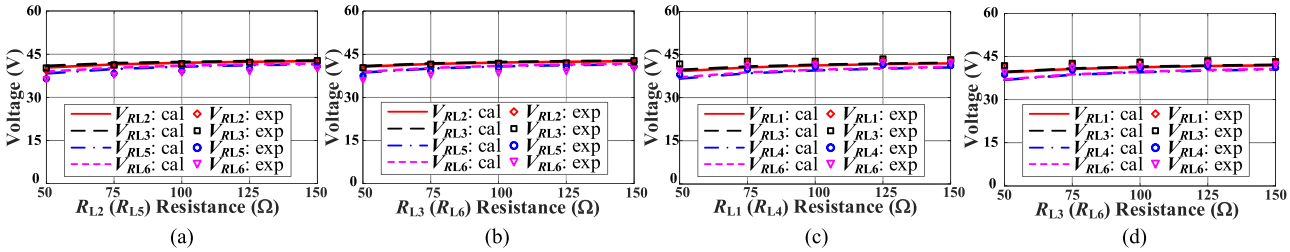

Fig. 12. Output voltage variations. (a) Mode 1: Varying R_{L2} and R_{L5}. (b) Mode 1: Varying R_{L3} and R_{L6}. (c) Mode 2: Varying R_{L1} and R_{L4}. (d) Mode 2: Varying R_{L3} and R_{L6}.

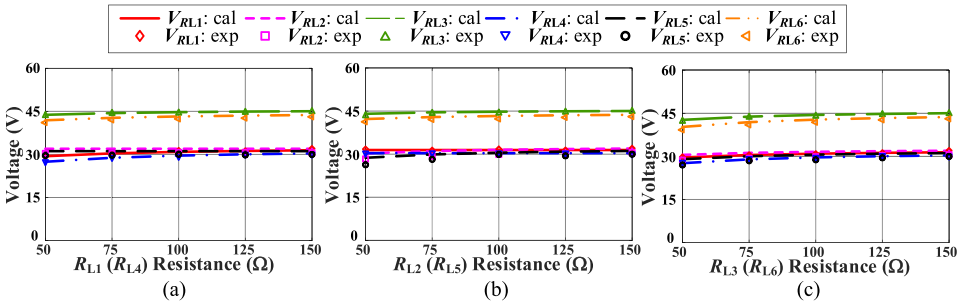

Fig. 13. Output voltage variations in Mode 3. (a) Varying R_{L1} and R_{L4}. (b) Varying R_{L2} and R_{L5}. (c) Varying R_{L3} and R_{L6}.

TABLE III
PARAMETERS OF THE EXPERIMENTAL SETUP

Symbol	Value	Symbol	Value	Symbol	Value
V_{INV}	50 V	f_1	200 kHz	f_2	272.7 kHz
R_{L}	50—150 Ω	L_{T1}	152.61 μH	L_{T2}	155.12 μH
L_{R1}	152.42 μH	L_{R2}	154.89 μH	M_1	45.92 μH
M_2	46.05 μH	L_1	31.03 μH	L_2	25.90 μH
L_3	31.05 μH	L_4	25.92 μH	L_{S1}	35.68 μH
L_{S2}	35.50 μH	L_{f1}	45.96 μH	L_{f2}	46.00 μH
C_{T1}	3.095 nF	C_{T2}	3.086 nF	C_{R1}	3.096 nF
C_{R2}	3.099 nF	C_1	20.47 nF	C_2	13.044 nF
C_3	20.36 nF	C_4	13.451 nF	C_{S1}	11.041 nF
C_{S2}	10.942 nF	C_{f1}	7.521 nF	C_{f1}	7.380 nF
Q_{T}, Q_{R}	200	Q_1	165	Q_2	115
Q_{S}	140	Q_{f}	100		

and the parameters of the final experimental setup are shown in Table III.

The calculated and experimental output voltages in three operating modes are shown in Figs. 12 and 13. To verify the feasibility of selective CV output in various cases, the following experiments are designed.

1) R_{L1} and R_{L4} are varied from 50 to 150 Ω; other loads are fixed at 150 Ω.
2) R_{L2} and R_{L5} are varied from 50 to 150 Ω; other loads are fixed at 150 Ω.
3) R_{L3} and R_{L6} are varied from 50 to 150 Ω; other loads are fixed at 150 Ω.

In Mode 1, R_{L1} and R_{L4} are not powered, and the load variation is meaningless, which can be discarded. R_{L2} and R_{L4} in Mode 2 are the same. Thus, these two situations are not discussed.

The load voltage varies with the load, and there is no definite reference value to evaluate the CV output. Define the rate of fluctuation of the output voltage as

$$\alpha = \frac{V_{\mathrm{OUT\_MAX}} - V_{\mathrm{OUT\_MIN}}}{V_{\mathrm{OUT\_MAX}} + V_{\mathrm{OUT\_MIN}}} \times 100\%. \tag{17}$$

In Mode 1, when R_{L2} and R_{L5} are varied from 50 to 150 Ω with the others assigned to 150 Ω, V_{RL2} increased from 39.22 to 42.51 V, V_{RL3} increased from 40.26 to 42.8 V, V_{RL5} increased from 36.47 to 40.79 V, and V_{RL6} increased from 36.67 to 40.35 V. α is 4.025%, 3.070%, 5.592%, and 4.778%, respectively. Any fluctuations in the output voltage are acceptable, and the constant output voltage is reached. In contrast, the maximum voltage of V_{RL1} and V_{RL4} is 1.57 V, which is significantly lower than the output voltages.

Similarly, in Mode 2, when R_{L1} and R_{L4} are varied from 50 to 150 Ω with the others assigned to 150 Ω, V_{RL1} increased from 40.32 to 43.07 V, V_{RL3} increased from 41.72 to 43.19 V, V_{RL4} increased from 38 to 41.14 V, and V_{RL6} increased from 39.86 to 42.75 V. α is 3.309%, 2.031%, 4.282%, and 3.545%, respectively. The maximum voltage of V_{RL2} and V_{RL5} is 1.15 V. As a result, the system can achieve selective power transfer by switching between the different modes.

The remaining results are given in Table IV. Regardless of which load changes, the system can maintain CV outputs and achieve selective output according to the operating mode.

Fig. 14 shows the experimental waveforms of different load branches in Mode 3. The waveforms of R_{L1} and R_{L4} contain only frequency f_2 components, and the waveforms of

TABLE IV
MEASURED OUTPUT VOLTAGES OF VARIOUS SITUATIONS

Working mode	Condition	V_{RL1} (V)	α (%)	V_{RL2} (V)	α (%)	V_{RL3} (V)	α (%)
Mode 1	$R_{L2}=R_{L5}=50-150\ \Omega$	0.72—1.17	–	39.22—42.51	4.03	40.25—42.80	3.07
	$R_{L3}=R_{L6}=50-150\ \Omega$	0.68—1.17	–	40.03—42.51	3.00	40.36—42.80	2.93
Mode 2	$R_{L1}=R_{L4}=50-150\ \Omega$	40.32—43.08	3.31	0.81—0.91	–	41.72—43.45	2.03
	$R_{L3}=R_{L6}=50-150\ \Omega$	41.68—43.32	1.93	0.85—0.92	–	41.81—43.52	2.00
Mode 3	$R_{L1}=R_{L4}=50-150\ \Omega$	19.52—21.36	4.50	20.25—20.50	0.61	28.95—29.86	1.54
	$R_{L2}=R_{L5}=50-150\ \Omega$	20.93—21.36	1.02	18.91—20.40	3.79	28.86—29.86	1.70
	$R_{L3}=R_{L6}=50-150\ \Omega$	19.86—21.36	3.64	19.14—20.40	3.19	28.08—29.86	3.07
Working mode	Condition	V_{RL4} (V)	α (%)	V_{RL5} (V)	α (%)	V_{RL6} (V)	α (%)
Mode 1	$R_{L2}=R_{L5}=50-150\ \Omega$	1.40—1.80	–	36.47—40.79	5.59	36.67—40.35	4.78
	$R_{L3}=R_{L6}=50-150\ \Omega$	1.34—1.77	–	37.54—40.79	4.15	36.35—40.35	5.22
Mode 2	$R_{L1}=R_{L4}=50-150\ \Omega$	38.00—41.40	4.28	0.93—1.15	–	39.86—42.79	3.55
	$R_{L3}=R_{L6}=50-150\ \Omega$	38.75—41.61	3.56	0.92—1.15	–	40.10—42.97	3.45
Mode 3	$R_{L1}=R_{L4}=50-150\ \Omega$	18.39—20.15	4.57	19.75—20.04	0.73	27.39—28.73	2.39
	$R_{L2}=R_{L5}=50-150\ \Omega$	20.15—20.37	0.54	17.55—19.99	6.50	27.52—28.73	2.15
	$R_{L3}=R_{L6}=50-150\ \Omega$	18.71—20.26	3.98	18.01—19.99	5.21	26.17—28.73	4.66

Note: load resistances not mentioned are fixed at 150 Ω.

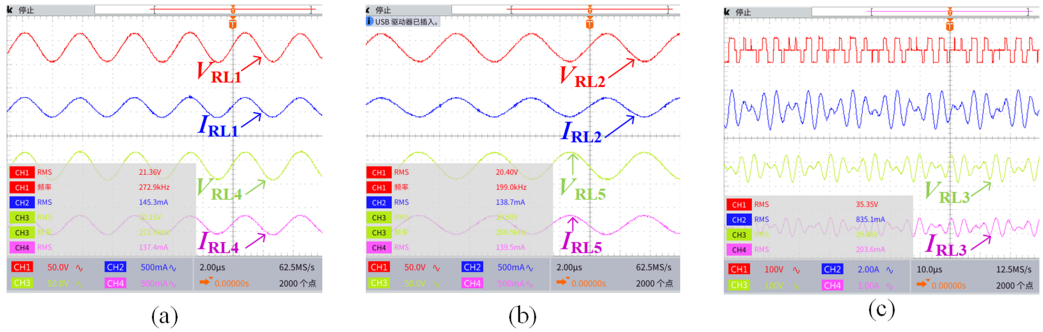

Fig. 14. Experimental waveforms. (a) Load branch passed frequency f_2. (b) Load branch passed frequency f_1. (c) Load branch passed both frequencies.

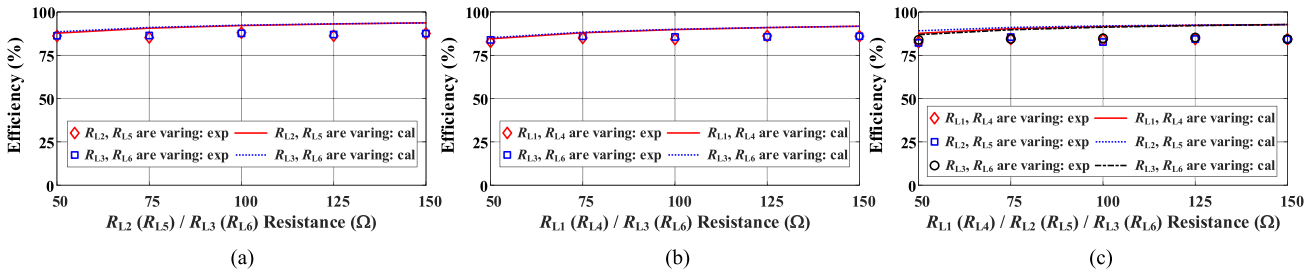

Fig. 15. Efficiency variations with different load resistances. (a) Mode 1. (b) Mode 2. (c) Mode 3.

R_{L2} and R_{L5} contain only frequency f_1 components, so the filter networks can handle the unwanted frequency components as well as the harmonic components from the inverter well.

Fig. 15 shows the system efficiency for each experiment group. The error is caused by the presence of parasitic impedance of the connection wires. It is easily obtained that the system can keep an efficiency of at least 82.19%, and the average efficiency is 85.23%. As load varies, the maximum change in system efficiency is 3.38%. These conclusions can demonstrate that the system can achieve a high stable efficiency.

Fig. 16 shows the output power for each experiment group. The output power increases when the load resistance decreases and achieves maximum of 85.95 W when R_{L3} and R_{L6} are 50 Ω in Mode 2.

Fig. 17 shows the waveforms of the inverter output voltage and the output current. ZPA is achieved at both the frequencies,

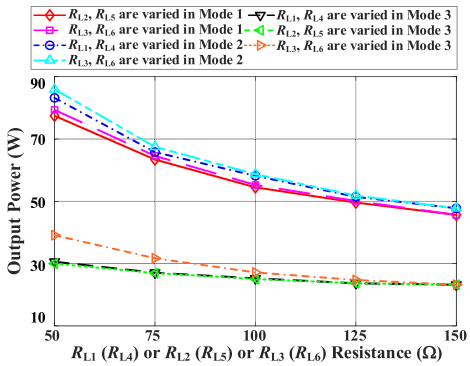

Fig. 16. Output power variations with various load changes in different modes.

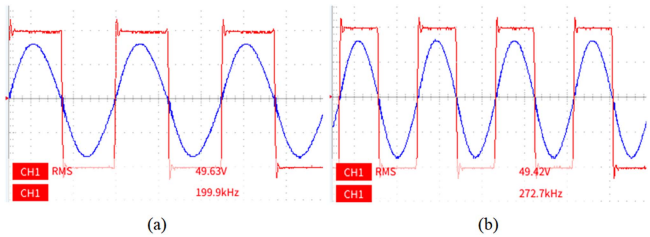

Fig. 17. Waveforms of inverter output voltage and output current at (a) 200 kHz and (b) 272.7 kHz.

which helps to reduce the switching losses and improve the power transfer capacity.

V. Conclusion

This article has proposed a modular single-channel dual-frequency WPT system to achieve multiple selective CV outputs with ZPA for APS. The system is adopted with working frequency located at its CV output points. The compensation network is designed to avoid cross interference and to achieve ZPA. The mathematical model of the proposed topology has been derived, and the resonant relationship has been analyzed. The magnetic coupler design principles have been proposed, and the self-decoupling characteristic of different shaped coils is utilized to realize magnetic integration. The multiple selective CV outputs have been verified in experiments. The selective power supply for different loads can be realized by changing the working frequency. The maximum output power of 85.95 W and the average transmission efficiency of 85.23% have been realized.

References

[1] Y. Wang, T. Li, M. Zeng, J. Mai, P. Gu, and D. Xu, "An underwater simultaneous wireless power and data transfer system for AUV with high-rate full-duplex communication," *IEEE Trans. Power Electron.*, vol. 38, no. 1, pp. 619–633, Jan. 2023.

[2] Y. Zhang, S. Chen, X. Li, and Y. Tang, "Design methodology of free-positioning nonoverlapping wireless charging for consumer electronics based on antiparallel windings," *IEEE Trans. Ind. Electron.*, vol. 69, no. 1, pp. 825–834, Jan. 2022.

[3] M. Wagih, A. Komolafe, I. Ullah, A. S. Weddell, and S. Beeby, "A wearable all-printed textile-based 6.78 MHz 15 W-output wireless power transfer system and its screen-printed joule heater application," *IEEE Trans. Ind. Electron.*, vol. 71, no. 4, pp. 3741–3750, Apr. 2024.

[4] Y. Zhang, Z. Shen, W. Pan, H. Wang, Y. Wu, and X. Mao, "Constant current and constant voltage charging of wireless power transfer system based on three-coil structure," *IEEE Trans. Ind. Electron.*, vol. 70, no. 1, pp. 1066–1070, Jan. 2023.

[5] R. Xie, Y. Wu, H. Tang, Y. Zhuang, and Y. Zhang, "A strongly coupled vehicle-to-vehicle wireless charging system for emergency charging purposes with constant-current and constant-voltage charging capabilities," *IEEE Trans. Power Electron.*, vol. 39, no. 4, pp. 3985–3989, Apr. 2024.

[6] G. Liu and B. Zhang, "Analytical model of a 25–50 m robust single-wire electric-field coupling power transfer system using a limiter," *IEEE Trans. Circuits Syst. II: Exp. Briefs*, vol. 66, no. 6, pp. 978–982, Jun. 2019.

[7] Y. Wu, H. Wang, Y. Zhuang, and Y. Zhang, "A shared charging channel for power and auxiliary batteries in electric vehicles," *IEEE Trans. Ind. Electron.*, vol. 71, no. 7, pp. 8202–8206, Jul. 2024.

[8] H. Kanazawa, H. Uwai, S. Kiuchi, and H. Matsumoto, "Receiver-position-based unbalanced-current control for a three- to single-phase wireless power transfer system for AGVs," *IEEE Trans. Ind. Electron.*, vol. 70, no. 4, pp. 3245–3256, Apr. 2023.

[9] Y. Zhang, C. Liu, M. Zhou, and X. Mao, "A novel asymmetrical quadrupolar coil for interoperability of unipolar, bipolar, and quadrupolar coils in electric vehicle wireless charging systems," *IEEE Trans. Ind. Electron.*, vol. 71, no. 4, pp. 4300–4303, Apr. 2024.

[10] N. Ha-Van, Y. Liu, P. Jayathurathnage, C. R. Simovski, and S. A. Tretyakov, "Cylindrical transmitting coil for two-dimensional omnidirectional wireless power transfer," *IEEE Trans. Ind. Electron.*, vol. 69, no. 10, pp. 10045–10054, Oct. 2022.

[11] W. Pan, C. Liu, H. Tang, Y. Zhuang, and Y. Zhang, "An interoperable electric vehicle wireless charging system based on mutually spliced double-D coil," *IEEE Trans. Power Electron.*, vol. 39, no. 3, pp. 3864–3872, Mar. 2024.

[12] H. Wang and K. W. E. Cheng, "Analysis, design, and validation of a decoupled double-receiver wireless power transfer system with constant voltage outputs for industrial power supplies," *IEEE Trans. Ind. Informat.*, vol. 19, no. 1, pp. 362–370, Jan. 2023.

[13] J.-H. Cho, S. Jung, and Y.-J. Kim, "Wireless power transfer for variable load, distance, and power division ratio in a loosely-coupled multiple-receiver relay system," *IEEE Trans. Ind. Electron.*, vol. 70, no. 7, pp. 6809–6818, Jul. 2023.

[14] C. Cheng, W. Li, Z. Zhou, Z. Deng, and C. Mi, "A load-independent wireless power transfer system with multiple constant voltage outputs," *IEEE Trans. Power Electron.*, vol. 35, no. 4, pp. 3328–3331, Apr. 2020.

[15] C. Cheng, Z. Zhou, W. Li, Z. Deng, and C. C. Mi, "A power relay system with multiple loads using asymmetrical coil design," *IEEE Trans. Ind. Electron.*, vol. 68, no. 2, pp. 1188–1196, Feb. 2021.

[16] Y. Zhang, T. Lu, Z. Zhao, F. He, K. Chen, and L. Yuan, "Selective wireless power transfer to multiple loads using receivers of different resonant frequencies," *IEEE Trans. Power Electron.*, vol. 30, no. 11, pp. 6001–6005, Nov. 2015.

[17] X. Tian, K. T. Chau, Z. Hua, and W. Han, "Design and analysis of demand-customized selective wireless power transfer system," *IEEE Trans. Ind. Electron.*, vol. 69, no. 12, pp. 13451–13461, Dec. 2022.

[18] X. Gao, B. Du, Y. Zhang, and S. Cui, "A dual-frequency compatible wireless power transfer system with a single transmitter and multiple receivers," *IEEE Access*, vol. 10, pp. 102564–102574, 2022.

[19] C. Cai, J. Wang, M. Saeedifard, P. Zhang, R. Chen, and J. Zhang, "Gyrator-gain variable WPT topology for MC-unconstrained CC output customization using simplified capacitance tuning," *IEEE Trans. Ind. Electron.*, vol. 71, no. 4, pp. 3594–3605, Apr. 2024.

[20] W. Pan, Z. Huang, C. Liu, R. Liu, H. Tang, and Y. Zhang, "A modular single-channel dual-frequency wireless power transfer system to achieve multiple selective constant-voltage outputs with zero phase plane," in *Proc. IEEE 18th Conf. Ind. Electron. Appl.*, 2023, pp. 563–567.

Wenxuan Pan was born in Shanxi, China. He is working toward the master's degree in power electronics with the School of Electrical Engineering and Automation, Fuzhou University, Fuzhou, China.

His research interests include wireless power transfer.

Zhongjin Huang was born in Fujian, China. He is working toward the master's degree in power electronics with the School of Electrical Engineering and Automation, Fuzhou University, Fuzhou, China.

His research interests include wireless power transfer.

Rongbin Liu was born in Fujian, China. He is working toward the master's degree in power electronics with the School of Electrical Engineering and Automation, Fuzhou University, Fuzhou, China.

His research interests include wireless power transfer.

Hongmin Tang was born in Fujian, China. He is working toward the master's degree in power electronics with the School of Electrical Engineering and Automation, Fuzhou University.

His research interests include wireless power transfer.

Ronghuan Xie (Graduate Student Member, IEEE) was born in Fujian, China. He is working toward the master's degree in power electronics with the School of Electrical Engineering and Automation, Fuzhou University, Fuzhou, China.

His research interests include wireless power transfer.

Yizhan Zhuang (Member, IEEE) was born in Fujian, China, in 1994. He received the B.S. degree in electrical engineering from the College of Electrical Engineering and Automation, Fuzhou University, Fuzhou, China, in 2017, and the Ph.D. degree in electrical engineering from the School of Electrical Engineering, Wuhan University, Wuhan, China, in 2023.

He is currently a Lecturer (Associate Researcher) with the School of Electrical Engineering and Automation, Fuzhou University. His research interests include dc–dc power converters and interface of photovoltaic conversion systems.

Yiming Zhang (Senior Member, IEEE) received the B.S. and Ph.D. degrees in electrical engineering from Tsinghua University, Beijing, China, in 2011 and 2016, respectively.

He was a Postdoctoral Researcher with San Diego State University, San Diego, CA, USA, and a Research Fellow with Nanyang Technological University, Singapore. He is currently a Full Professor with Fuzhou University, Fuzhou, China. He has authored one book from Springer and authored or coauthored more than 100 technical papers in journals and conference proceedings. His research interests include wireless power transfer and resonant converters.

Dr. Zhang was the recipient of the Outstanding Doctoral Dissertations of Tsinghua University in 2016. He was recognized as an Outstanding Reviewer for IEEE TRANSACTIONS ON POWER ELECTRONICS in 2019 and 2022 and a Distinguished Reviewer for IEEE TRANSACTIONS ON INDUSTRIAL ELECTRONICS in 2020. He was the Publication Chair of International Conference on Wireless Power Transfer 2022.